

---

---

Contract # 693JK31910017POTA

# **GPR MAPPING ROBOT FINAL PUBLIC REPORT**

AUTHOR(S): BAIYANG REN, VINEET PANDEY, AALAP SHAH

CONTROL NUMBER: GPR-TR-003P

DATE: FEBRUARY 4, 2022

VERSION: FINAL PUBLIC REPORT, REV. A

## **Revision History**

<b>Modified By</b>	<b>Modified Date</b>	<b>Reason for Modification</b>	<b>Version</b>
A. Shah, B. Ren, V. Pandey	2/4/2022	Final Public Report	Rev A

Name: GPR Mapping Robot, Final Public Report	Version: Final, Rev. A
Document ID: GPR-TR-003P	Date: 2/4/2022

**TABLE OF CONTENTS**

**SECTION..... PAGE**

List of Tables..... iv

List of Figures ..... iv

**1 INTRODUCTION.....6**

**2 OVERVIEW .....6**

**3 BACKGROUND.....7**

**4 PROPOSED WORK .....9**

**5 SIMULATION RESULTS .....9**

5.1 3D MIGRATION.....9

5.2 MULTI-STATIC DATA COLLECTION .....12

5.3 ANTENNA POLARIZATION .....15

5.4 SUMMARY .....18

**6 SYSTEM DESIGN.....18**

6.1 AUTONOMY IN GPR ANTENNA SCANNING .....21

6.2 GRAPHICAL USER INTERFACE .....21

6.3 GPR DATA VISUALIZATION .....22

6.4 LOCALIZATION .....23

6.5 NAVIGATION .....24

6.5.1 LOCAL AND GLOBAL COSTMAP .....24

6.5.2 LOCAL AND GLOBAL PLANNER .....24

6.5.3 RECOVERY BEHAVIOR .....24

**7 TESTING AT MOCK ROADWAY .....25**

7.1 MOCK ROADWAY CONSTRUCTION .....25

7.1.1 MOCK ROADWAY # 1.....25

7.1.2 MOCK ROADWAY #2.....26

7.2 TESTING RESULTS .....27

7.2.1 COMMON-OFFSET MODE .....27

7.2.1.1 RESULTS ON MOCK ROADWAY #1 .....27

7.2.1.2 RESULTS ON MOCK ROADWAY #2 .....31

7.2.2 MULTI-STATIC MODE.....33

7.3 SUMMARY .....33

7.4 FUTURE WORK.....34

**8 REFERENCES .....35**

Glossary of Acronyms and Abbreviations ..... vi

Name: GPR Mapping Robot, Final Public Report	Version: Final, Rev. A
Document ID: GPR-TR-003P	Date: 2/4/2022

**LIST OF FIGURES**

Figure 1: Different GPR Survey Types Conducted by ULC..... 7

Figure 2: Different Tx-Rx Orientation Configurations. The arrow shows the direction of the scanning path. The bowtie antenna in the Tx or Rx dictates the antenna’s polarization. (a) Parallel, Co-polarized, End-fire (b) Parallel Co-polarized, Broadside (c) Parallel, Cross-polarized (d) Perpendicular, Co-polarized, End-fire (e) Perpendicular, Co-polarized, Broadside (f) Perpendicular, Cross-polarized..... 8

Figure 3: An Illustration of the Typical GPR Configuration for Utility Locating ..... 8

Figure 4. A Model with Four Metallic Pipes of Different Orientations..... 10

Figure 5. Raw Data Shown as a Point Cloud. .... 10

Figure 6. (a)The stacked 2D migration and (b) 3D migration results are shown as point cloud plots.11

Figure 7. 3D migration results using different spacing in the Y direction. .... 12

Figure 8. The sketch of the model for the multi-static study..... 13

Figure 9. The comparison between the results of (a) Common-Offset and (b) Multi-Static data. The amplitude at the 1<sup>st</sup> layer is shown in (c). .... 14

Figure 10. The comparison between the results of (a) Common-Offset and (b) Multi-Static data. The amplitude at the 2<sup>nd</sup> layer is shown in (c). .... 14

Figure 11. A sample B-scan of the common-offset data using Y-Y polarization. .... 15

Figure 12. A-scans of the four polarizations. .... 16

Figure 13. 3D migration results of the four polarizations. .... 17

Figure 14. The vector field is produced by combining different polarizations of Tx and Rx..... 17

Figure 15 GPR Mapping Robotic System..... 18

Figure 16. The movement of antenna in the common offset mode. Tx: blue, Rx, yellow. .... 19

Figure 17. The movement of antenna in the multi-static mode. Tx: blue, Rx, yellow..... 20

Figure 18: Back Side of Robot: Showing Batteries ..... 21

Figure 19: Data Processing tab showing GUI components for two layers..... 22

Figure 20: 3D point cloud of the mapped utility - Visualization window..... 22

Figure 21: Mapped parking-lot at ULC facility using Google Cartographer..... 23

Figure 22. The design map of Mock Roadway #1. .... 25

Figure 23: The pipe layout of ULC’s mock roadway #2. The pipes numbering scheme is shown in Table 1 ..... 26

Figure 24. The result in the point cloud format..... 28

Figure 25. C-scan results at different depths..... 28

Figure 26. The point cloud results from 2D migration for the 3<sup>rd</sup> scan at site #2 with (a) dy=0.05m and (b) dy=0.15m..... 29

Name: GPR Mapping Robot, Final Public Report	Version: Final, Rev. A
Document ID: GPR-TR-003P	Date: 2/4/2022

Figure 27. C-scan results from 3D migration at different depths..... 30

Figure 28. C-scan results from 2D migration (dy=0.15m) at different depths..... 31

Figure 29. The 3D migration results in the point cloud format..... 32

Figure 30. C-scan results from 3D migration at different depths..... 32

Figure 31. Comparison between the results from common-offset and multi-static data collection in real and absolute values..... 33

Name: GPR Mapping Robot, Final Public Report	Version: Final, Rev. A
Document ID: GPR-TR-003P	Date: 2/4/2022

## 1 INTRODUCTION

The Pipeline and Hazardous Materials Safety Administration (PHMSA) awarded ULC Technologies (ULC) the project titled – “Improving Subsurface Non-Metallic Utility Locating using Self-Aligning Robotic Ground Penetrating Radar”. This report details the work performed under this project and the future tasks that will be carried out to make this product commercial-ready.

Ground Penetrating Radar (GPR) has been extensively used for mapping and locating underground pipelines and preventing third-party damages. However, commercially available radars are less effective when attempting to detect non-metallic pipelines. This has resulted in incorrect maps for underground utilities and larger excavation sites to repair the utilities resulting in high repair costs. In addition, not being able to detect underground utilities can result in excavation damage. Hence, ULC designed and developed a GPR-based robotic system that uses a dual antenna system to collect larger amounts of data at finer resolution than the state-of-art. The system utilizes advanced signal processing algorithms to process the GPR dataset for improved detection, reduced false negatives, and more accurate maps of the sub-surface for both metallic and non-metallic buried utilities.

## 2 OVERVIEW

A semi-autonomous robotic wheeled platform was designed and developed that can be transported by a small truck across roads and then driven by an operator locally to the locating or surveying location. Using a lightweight, handheld console, the operator can command the robot to perform an automated scan routine. The robot employs a dual antenna system with multiple degrees of freedom to adjust antenna polarization angles and perform different scanning modes. The most preferred are the Common Offset Mode and Multi-Static Mode. Motors and encoders perform precise positioning of the antennas. Additional sensors and a localization algorithm provide accurate coordinates to locate the asset confidently. Algorithms were implemented for Synthetic Aperture Focusing and generating images, including B-scan, C-scan, and point clouds.

ULC built a realistic test site specifically to challenge the robot’s capabilities for plastic pipe detection. Testing was performed at two of ULC’s test sites. The testing results showed significant improvements in the ability to detect and locate both metallic and non-metallic pipelines and the ability to detect other utilities and structures such as a conduit duct bank and electrical cable conduits. When compared with the conventional approach of manual operator pushcarts, it is clear that a robot can collect more data with higher accuracy and resolution and can do so reliably and consistently. The ability to program a robot allows for various scanning modes and flexibility during the scanning.

Although design and sensor selection was completed for collision avoidance and automated mark out, this was not implemented and can be incorporated in the future. The robotic system developed under this project should be tested at customer sites, and the system performance should be enhanced through learnings from these tests and customer feedback. When fully developed as a product, the system will reduce human-related errors and training needs while improving the detection of plastic and metallic pipes. If ULC can successfully deploy this as a service for locating and mark out, ULC envisions a reduction in third-party excavation damage.

Name: GPR Mapping Robot, Final Public Report	Version: Final, Rev. A
Document ID: GPR-TR-003P	Date: 2/4/2022

### 3 BACKGROUND

Traditional mark-out often relies on using out-of-date records to locate target assets, resulting in third-party damage. This is typically the case when pipe locating equipment fails to detect the buried target pipeline or surrounding utilities. Third-party damage is expensive to remediate, may lead to hazardous conditions that could affect people and property, and may result in disruption to customers. Pipeline operators are seeking better methods and technologies to locate pipe in varying soil conditions, in congested areas, and specifically to locate non-metallic pipe. Table 1 shows that, in 2018, 40% of all the natural gas mains in the US were steel, and 58% were plastic. Only 23% were steel for natural gas services while 74% were plastic. Using conventional locating technologies, locating plastic pipes requires innovations and new methods to improve the detectability, characterization, and classification of target pipes and surrounding objects.

Pipe Material	Calendar Year	MAIN		SERVICES	
		Total Miles	% of Miles	Total Miles	% of Miles
STEEL	2018	525,467.2	40.40	211,277.6	22.74
	2017	531,639.0	41.01	219,527.4	23.68
	2016	537,152.8	41.75	227,599.7	24.64
PLASTIC	2018	750,635.6	57.71	686,261.1	73.86
	2017	738,162.3	56.95	677,645.5	73.09
	2016	721,426.2	56.07	666,115.8	72.12

Table 1 Natural gas pipeline makeup in the U.S. ((Data Source: US DOT Pipeline and Hazardous Materials Safety Administration, <https://hip.phmsa.dot.gov/analyticsSOAP/saw.dll?Portalpages>)

Electromagnetic (EM) locating is a widely used underground locating technique. However, for non-conductive pipe, an intact tracing wire and direct access to the pipe are required. This is not usually satisfied in the field, and hence, for non-metallic, non-conductive pipes, this method is not useful. Ground Penetrating Radar (GPR) uses reflected/scattered electromagnetic waves to locate subsurface objects and has proven to be the most promising technique. This method is non-intrusive, requiring neither excavation nor access to the pipe. Before starting this project, ULC reviewed, tested, and evaluated commercially available GPR survey systems and found several deficiencies across all GPR products. These are:

1. The design and construction of most commercial utility locating GPR systems entail using a common offset antenna survey type that has several disadvantages compared to common mid-point, common transmitter, and common receiver antenna surveys. Figure 1 illustrates the difference in operation for these different types of survey types. The common offset type is widely used since it is easier for manually positioning the antennas during scanning, but provides less accurate wave speed measurement, lower Signal-to-Noise Ratio (SNR), decreased depth of penetration, and less accurate spatial positioning.

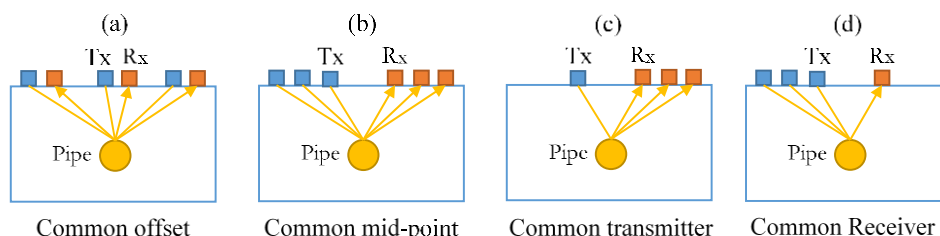


Figure 1: Different GPR Survey Types Conducted by ULC

2. Figure 2 illustrates several different antenna orientations. In most commercial GPR systems, the transmitter (Tx) and receiver (Rx) antennas are configured as co-polarized, perpendicular to scanning path, and broadside, as shown in Figure 2 (e). This orientation is desirable only when simple subsurface conditions prevail, such as when only one cylindrical pipe crosses the scanning path, as shown in Figure 3(a). The orientation does not perform so well in more complex conditions, e.g., multiple pipelines crossing each other at varying angles. Using different Tx-Rx orientations shown in Figure 2 can help to improve SNR and resolution in complex environments.

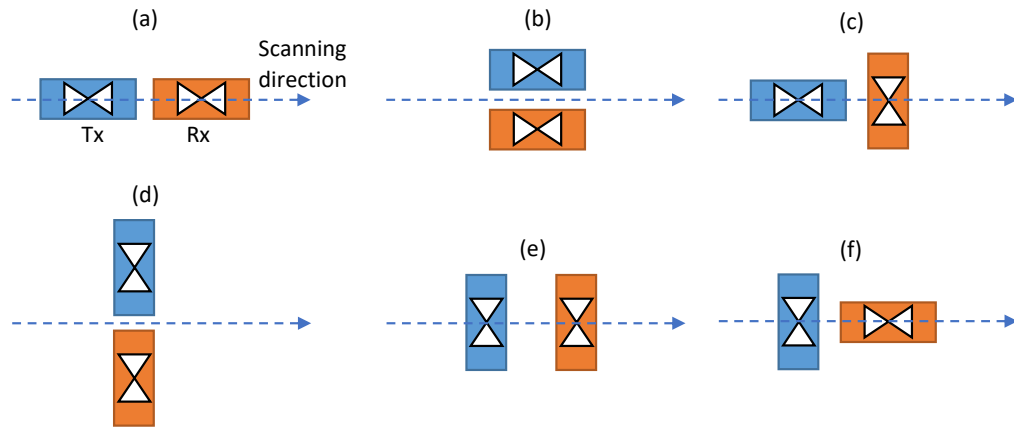


Figure 2: Different Tx-Rx Orientation Configurations. The arrow shows the direction of the scanning path. The bowtie antenna in the Tx or Rx dictates the antenna's polarization. (a) Parallel, Co-polarized, End-fire (b) Parallel Co-polarized, Broadside (c) Parallel, Cross-polarized (d) Perpendicular, Co-polarized, End-fire (e) Perpendicular, Co-polarized, Broadside (f) Perpendicular, Cross-polarized.

3. Current GPR survey procedures are time-consuming since the antenna is translated in a grid pattern, and there is no opportunity for refining the scanning path during manual scanning. The resolution (distance between parallel scan lines) that needs to be achieved to use advanced signal processing algorithms cannot be achieved by an operator. As shown in Figure 3(b), the grid pattern scanning enables detection of the pipes normal to the scanning path but may have low sensitivity and resolution for the two angled pipes.

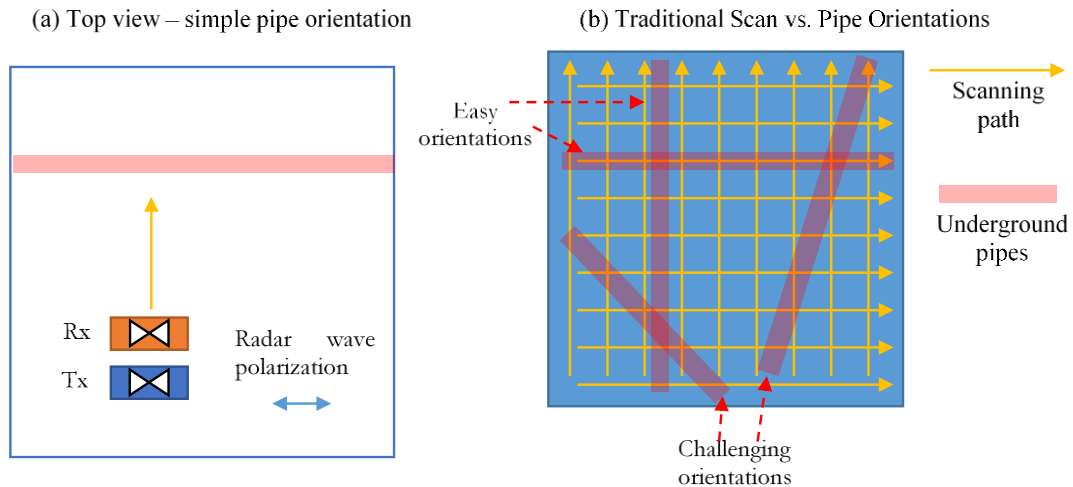


Figure 3: An Illustration of the Typical GPR Configuration for Utility Locating

Name: GPR Mapping Robot, Final Public Report	Version: Final, Rev. A
Document ID: GPR-TR-003P	Date: 2/4/2022

## 4 PROPOSED WORK

The initiative of this project was to improve the detectability of non-metallic pipelines. GPR depends on the reflection of electromagnetic waves to detect targets. Non-metallic pipes are difficult to detect because of their low reflectivity. Usually, the reflection depends on both the geometry and material of the reflector. Since pipes are cylinder-shaped, the reflectivity solely depends on the contrast between soil and pipe material, given that the pipe diameter is the same. The pipe material includes both pipe wall material and the media inside the pipe. In fact, for the gas pipelines, the gas inside the pipe provides the most significant contrast to the soil and makes the most contribution to the reflection. Similarly, the air inside the sewer pipe and water inside the water pipe play the leading role in GPR detection.

In the real world, the materials of soil and pipes are predetermined and cannot be changed. It is not likely that there is a way to increase the reflectivity of the non-metallic pipe due to its physical nature. A promising way to enhance the detectability of non-metallic pipes is to improve the overall performance of the GPR system. This will invariably improve the sensitivity to both metallic and non-metallic pipes.

The goal of the R&D efforts was thus to improve GPR performance for targets of any materials by employing non-conventional data collection methods and advanced signal processing techniques. In the following sections, some studies are illustrated by using metallic targets. However, it should be a reasonable expectation that improving the detectability of metallic targets will also translate to that for non-metallic pipes.

To achieve this goal, the following data collection methods were explored:

1. Fine grid scan for 3D migration. This will improve the performance when the scanning line is not perpendicular to the pipe.
2. Multi-static data collection. This will improve the detection of low-reflectivity targets by stacking multiple interrogations from different view angles.
3. Full polarization data collection. The polarity of the target could be revealed, which provides a novel way of viewing the underground targets.

The detailed results of using different methods will be presented and discussed in the following sections.

## 5 SIMULATION RESULTS

To illustrate the value and details of the proposed methods, a study using a numerical simulation tool was conducted. The simulation was performed using the open-source software `gprMax`[1, 2].

### 5.1 3D MIGRATION

This section presents the numerical results of fine grid scan and 3D migration [3].

A model was created such that four metallic pipes were buried in the sand soil ( $\epsilon_r = 4$ ) with different orientations, as shown in Figure 4(a). The red lines in Figure 4(b) show the scanning directions. The leftmost pipe has the ideal orientation respective to the scanning direction and is defined as  $0^\circ$ . The other three pipes are  $15^\circ$ ,  $30^\circ$ , and  $45^\circ$  relative to the ideal orientations. The diameter of all the pipes is 100mm. A point voltage source was used to simulate the transmitter antenna, and a point reading was used to simulate the receiver antenna. The data was collected as a common-offset antenna pair by moving both transmitter and receiver simultaneously to scan multiple lines. The scanning grid is 0.05m in both X and Y directions. It should be noted that maintaining 0.05m spacing between parallel lines is difficult for a human operator in the real world.

Name: GPR Mapping Robot, Final Public Report	Version: Final, Rev. A
Document ID: GPR-TR-003P	Date: 2/4/2022

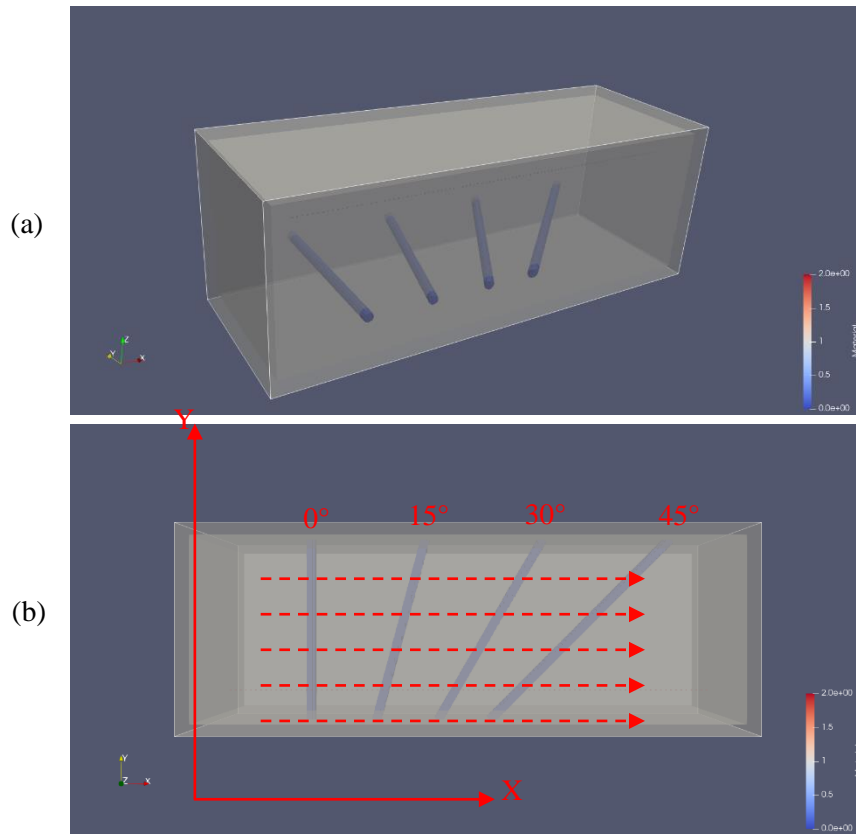


Figure 4. A Model with Four Metallic Pipes of Different Orientations.

The collected raw data was a group of temporal waveforms, i.e., A-scans, collected at different locations. The midpoint between Tx and Rx was used as the location of the waveform. The time axis was converted to depth using the speed of EM wave and placed as the Z-axis. As a result, a 3D dataset was generated with X- and Y-grid corresponding to antenna location, Z-axis corresponding to the depth, and the amplitude of each data point corresponding to received signal strength. By setting a threshold of the amplitude, only the large amplitudes were kept, and a representation in the style of point cloud is generated. The point cloud is shown in Figure 5. The hyperboloids correspond to the four pipes.

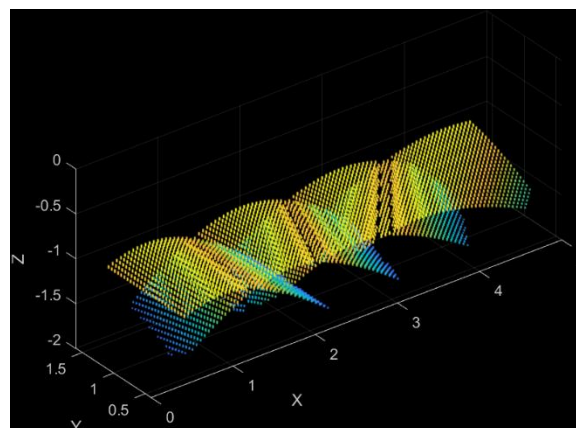


Figure 5. Raw Data Shown as a Point Cloud.

Name: GPR Mapping Robot, Final Public Report	Version: Final, Rev. A
Document ID: GPR-TR-003P	Date: 2/4/2022

In conventional data processing, each XZ plane is treated separately as a B-scan. The imaging algorithm, also called migration, is conducted for each B-scan. To represent the pipe as a 3D geometry, multiple migrated B-scans were stacked to produce a migrated 3D dataset. Similarly, the 3D dataset is presented in the point cloud format in Figure 6(a). It is noted that only the 0° pipe was imaged correctly. All three other pipes were “flattened” because the focusing algorithm did not function successfully. The worst-case was the 45° pipe where the reflected signal was still distributed across the 3D space. This will compromise the detectability of the pipe when the noise level is higher in the real world and induce difficulty in locating the pipe. On the other hand, the 3D dataset was processed using the 3D migration method to produce another point cloud shown in Figure 6(b). All four pipes were correctly imaged. The shapes of the pipes were not distorted. The 3D migration algorithm is independent of the pipe orientation and always guarantees the correct focusing is conducted. These features will empower its application with a better chance of success in the unknown real world.

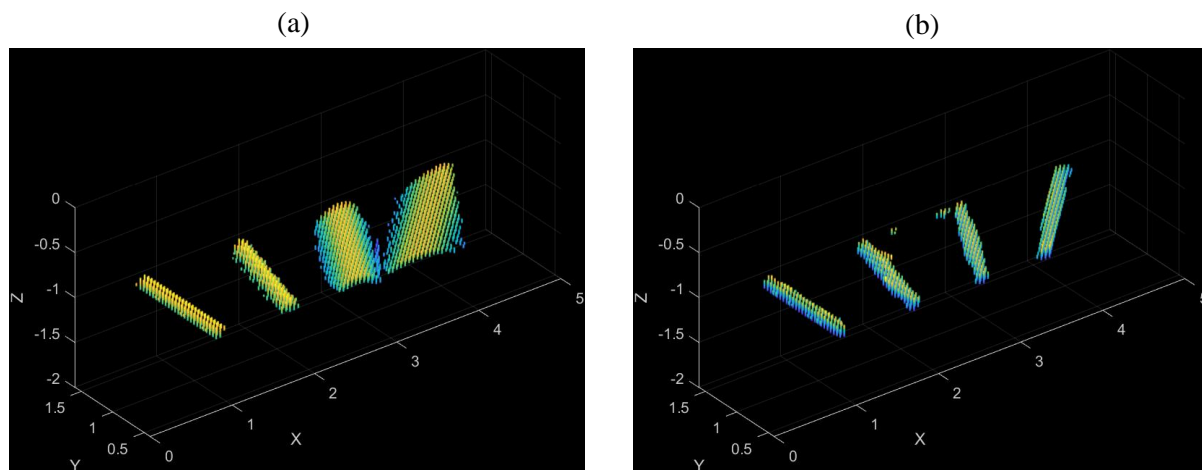


Figure 6. (a)The stacked 2D migration and (b) 3D migration results are shown as point cloud plots.

It should be emphasized that the 3D migration requires the spacing of the grid to be small enough and no greater than the half wavelength of the smallest wavelength of interest. The 3D raw dataset was resampled into datasets of different spacing in the Y direction to demonstrate the requirement. The spacing in the X direction was kept the same. Then, the 3D migration was applied to the three datasets, and the migrated results are shown in Figure 7. At 500 MHz and the wave speed of  $1.5e8$  m/s, the half-wavelength is 0.15m. The result of  $dy=0.05$  satisfied this requirement, and the focusing was accurate. The result of  $dy=0.15$  was right on the boundary, and only a bit of noise was observed around the 3<sup>rd</sup> pipe. It was seen that the result for  $dy=0.25$ m was heavily distorted. This was the result of aliasing because of too large sampling spacing. For example, for a typical clayey soil, the relative permittivity is around nine, and the half-wavelength is 0.1m. For the soils with larger permittivity, the wavelength gets even smaller. Maintaining such small spacing accurately is difficult for a pushing cart. A robotic system is needed to provide the desired accuracy and resolution.

Name: GPR Mapping Robot, Final Public Report	Version: Final, Rev. A
Document ID: GPR-TR-003P	Date: 2/4/2022

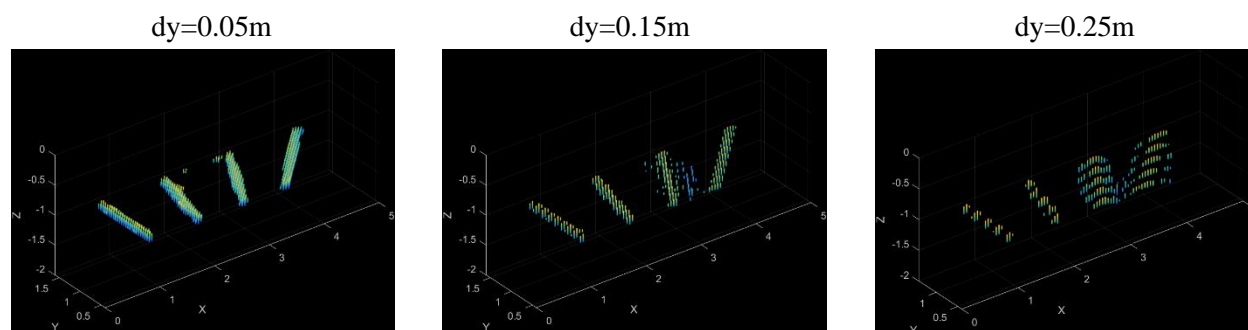


Figure 7. 3D migration results using different spacing in the Y direction.

## 5.2 MULTI-STATIC DATA COLLECTION

Nowadays, most GPR survey is conducted using the common-offset mode because it makes a reasonable compromise among the quality of data, the time consumption for data collection, and the complexity and cost of the system. Unfortunately, the common-offset GPR may not find all the assets when the underground environment is complicated due to the high congestion in urban areas. It is worth exploring a method that has better suitability to the complex environment.

The multi-static data collection requires the Tx and Rx can move independently to different locations. This study employs Full Matrix Capture (FMC) to get a complete set of Tx-Rx position combinations. To explain the FMC, assuming an XZ plane needs to be scanned, and N positions in a line are selected at the ground surface, Tx fires in turns at every position. At each Tx firing, Rx receives signals at all the N positions. Eventually, there are N x N Tx-Rx combinations in total. If the position for Tx and Rx are differently distributed, for example, Tx fires at M equally spaced positions and Rx receives at N equally spaced positions. There would be M x N Tx-Rx combinations. Common mid-point, common transmitter, and common receiver modes are subsets of the FMC and can be extracted if needed. In this report, if not noted explicitly, the FMC is used whenever the multi-static data collection is mentioned and discussed. The multi-static data collection is implemented by the robotic GPR antenna platform, which will be described in detail in the next chapter, System Design.

This numerical study assumed identical locations for Tx and Rx, i.e., N x N matrix. Eleven hollow pipes were buried at two layers at different depths. All the pipes were High-Density Polyethylene (HDPE) pipes with 100mm diameter. The goal of the two-layer configuration was to create a “blocking the view” scenario. The grid size was 0.025m. The locations spanned from 0.1m to 4.9m, and there are 193 x 193 Tx-Rx combinations in total. The transmitter and receiver settings are the same as those used in the previous section. The algorithms used for multi-static data processing are well explained in these papers [4, 5].

Name: GPR Mapping Robot, Final Public Report	Version: Final, Rev. A
Document ID: GPR-TR-003P	Date: 2/4/2022

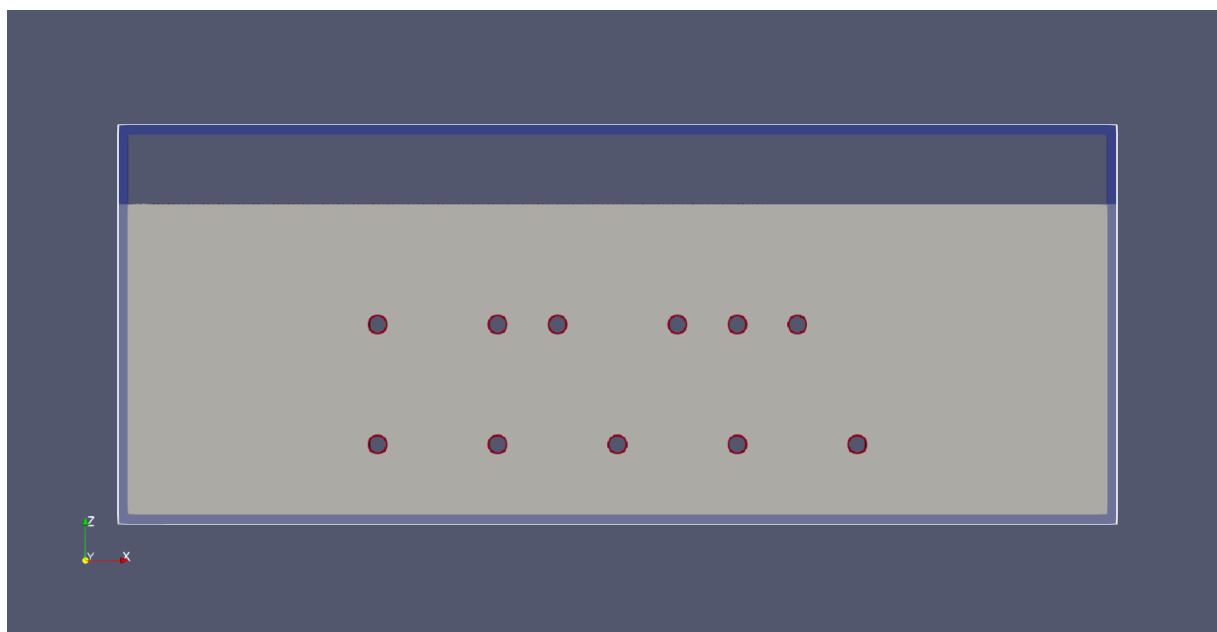


Figure 8. The sketch of the model for the multi-static study.

A subset of the collected data was used to create a common-offset dataset. The imaging result is shown in Figure 9(a). The full multi-static dataset was also used for imaging, and the results are shown in Figure 9(b). The amplitude at the depths of the two layers was extracted and plotted in Figure 9(c) and Figure 10(c). By comparing Figure 9(a) and (b), it was found that there are fewer imaging artifacts in (b) than in (a). This is evident when the depth was deeper than the 1<sup>st</sup> layer. This is because the 1<sup>st</sup> layer could block the view and cause multi-reflection among pipes. The result from the multi-static dataset was cleaner because the area under the 1<sup>st</sup> layer was imaged from different view angles (Tx-Rx locations), and the artifacts will be averaged out. Figure 9(c) shows that the two datasets have similar imaging performance for the 1<sup>st</sup> layer of pipes. However, Figure 10(c) shows some imaging artifacts are generated at the position without any reflector when the common-offset data is used.

Name: GPR Mapping Robot, Final Public Report	Version: Final, Rev. A
Document ID: GPR-TR-003P	Date: 2/4/2022

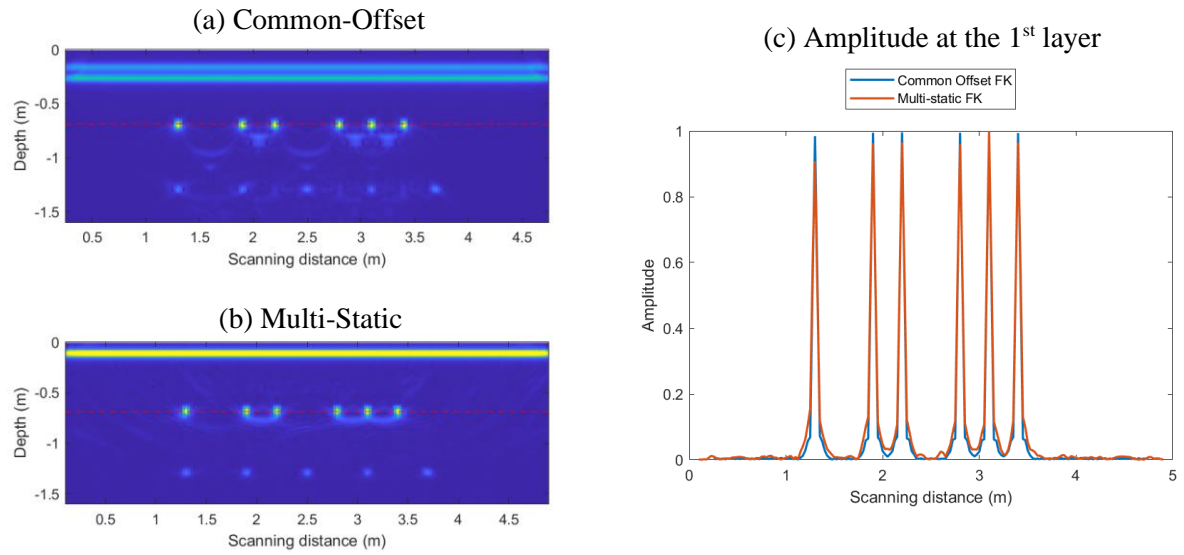


Figure 9. The comparison between the results of (a) Common-Offset and (b) Multi-Static data. The amplitude at the 1<sup>st</sup> layer is shown in (c).

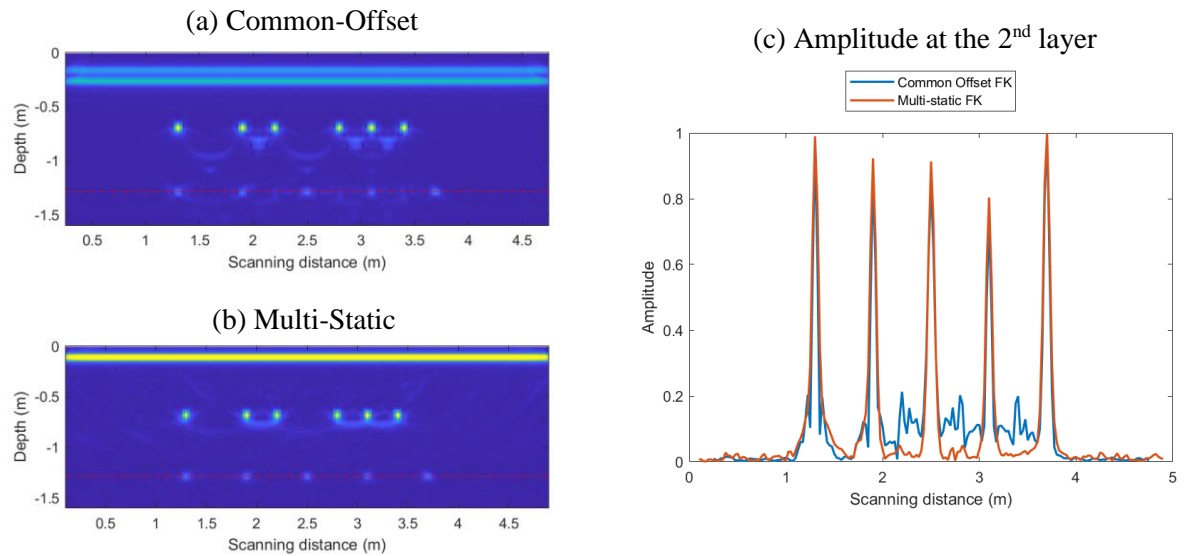


Figure 10. The comparison between the results of (a) Common-Offset and (b) Multi-Static data. The amplitude at the 2<sup>nd</sup> layer is shown in (c).

Name: GPR Mapping Robot, Final Public Report	Version: Final, Rev. A
Document ID: GPR-TR-003P	Date: 2/4/2022

### 5.3 ANTENNA POLARIZATION

To study the antenna polarization as an option for better imaging, the model in Figure 4 is used. The polarization of the transmitter and the receiver are set to X and Y direction independently. As a result, there are four combinations of polarizations of Tx and Rx, respectively, namely X-X, X-Y, Y-X, and Y-Y. The data collection is conducted at the same locations used for the 3D migration study.

A sample B-scan collected by Y-Y polarization is shown in Figure 11. The four hyperbolas correspond to  $0^\circ$ ,  $15^\circ$ ,  $30^\circ$ , and  $45^\circ$  respectively. The four black dash lines correspond to the central locations of the pipes. By plotting the A-scans at the four lines, Figure 12(d) is created. Interestingly, the reflection signal amplitude increases slightly as the offset angle increases. By plotting the other three polarizations, Figure 12(a), (b), and (c) are produced. The first reflected wave packets are highlighted by the red boxes. When polarizations of Tx and Rx are the same, the reflected signal is strong, and when different, the reflected signal is weak. In Figure 12(b) and (c), the  $0^\circ$  pipe produces almost zero reflection. The amplitude reflection increases as the offset angle increases. This indicates that the cross-polarization, X-Y and Y-X, is more sensitive to angled targets.

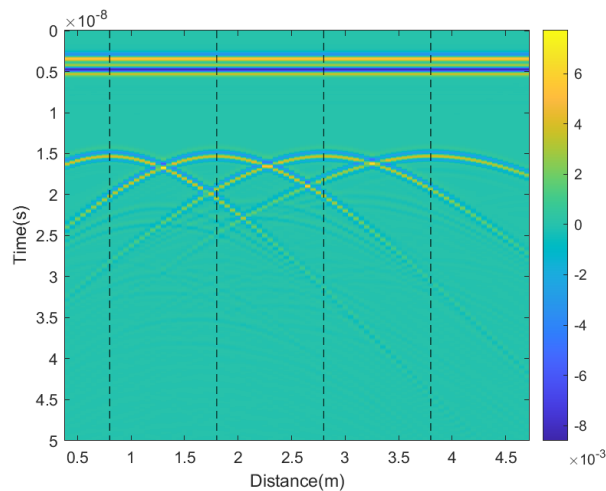


Figure 11. A sample B-scan of the common-offset data using Y-Y polarization.

Name: GPR Mapping Robot, Final Public Report	Version: Final, Rev. A
Document ID: GPR-TR-003P	Date: 2/4/2022

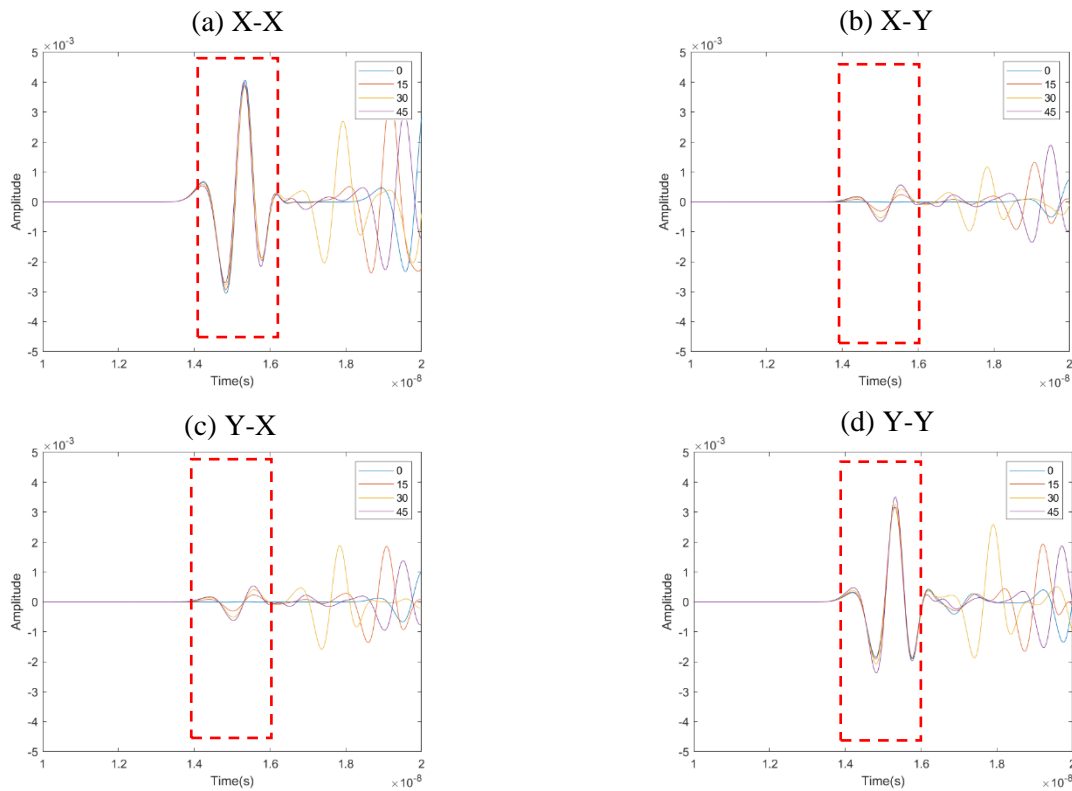


Figure 12. A-scans of the four polarizations.

By conducting the 3D migration with the inputs of 4 polarizations, the focused imaging was produced in Figure 13. The X-X and Y-Y results detected all four pipes, and the X-Y and Y-X results detected only the angled pipes.

If the migrated results of 4 polarizations are combined to form a scatter matrix, the orientations of the pipe can be calculated as an angle and a principal value[6, 7]. A vector field can be constructed using the principal value as the length of the vector and angle as the direction of the vector. A cross-section at a depth of the pipe is shown in Figure 14. It is observed that the four pipes are not only detectable by high amplitude, i.e., big arrow vectors, but also reveal their orientations. The vector field could be helpful to differentiate pipes from non-target objects. Since a pipe is a slender object, it will show a strong and consistent vector field over its volume. However, non-target objects and noise may have random vector fields.

Name: GPR Mapping Robot, Final Public Report	Version: Final, Rev. A
Document ID: GPR-TR-003P	Date: 2/4/2022

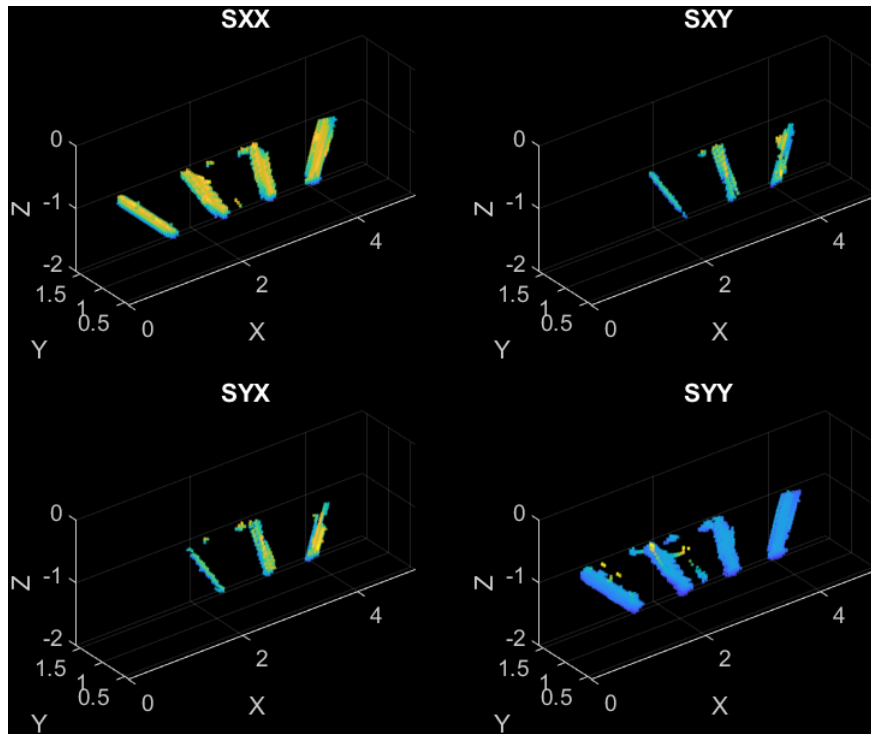


Figure 13. 3D migration results of the four polarizations.

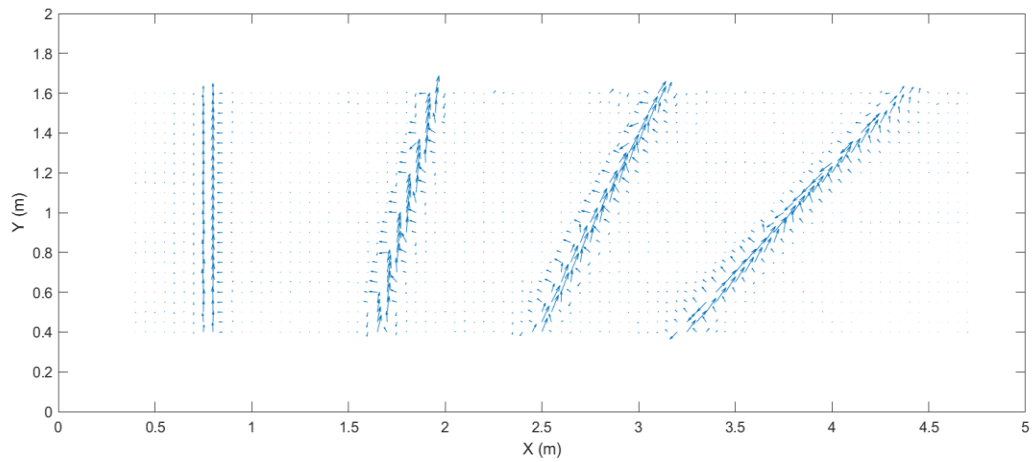


Figure 14. The vector field is produced by combining different polarizations of Tx and Rx.

Name: GPR Mapping Robot, Final Public Report	Version: Final, Rev. A
Document ID: GPR-TR-003P	Date: 2/4/2022

## 5.4 SUMMARY

In summary, three numerical studies demonstrated the capability and potential of using non-conventional scanning methods. The highlighted conclusions are:

- 3D migration is independent of pipe orientations and can deal with the unknown environment and increase the detectability of randomly oriented pipes.
- The grid size needs to be small enough, less than half of the smallest possible wavelength, to result in accurate 3D migration results.
- The multi-static data collection could increase the GPR imaging performance in complicated conditions.
- Common-offset and multi-static data have a similar capability to image the simple configuration.
- The orientation of the pipe can be revealed by processing the full-polarimetric signals. The vector field could be a helpful tool to differentiate pipe from non-target objects and noise.
- Conducting the scanning of the abovementioned data collection is either time-consuming or nearly impossible with the pushing cart-type GPR survey. A robotic system is needed to achieve accuracy, resolution, and automation.

## 6 SYSTEM DESIGN

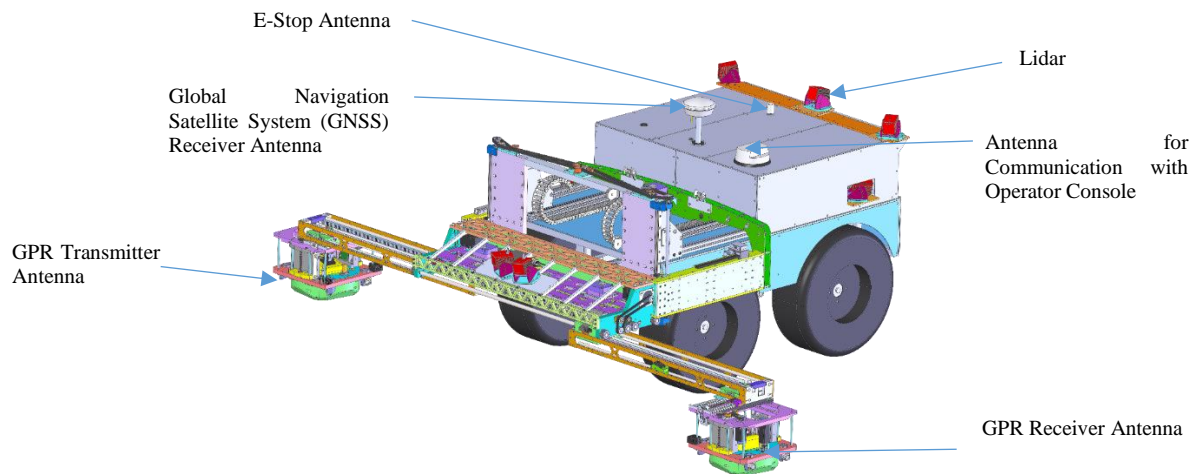


Figure 15 GPR Mapping Robotic System

A 3D isometric view of the robot is shown in Figure 15 and is composed of two major sub-systems:

- 1) GPR Antenna Platform
- 2) Mobile Platform

The **GPR antenna platform** has been designed to manipulate the GPR transmitter and receiver antennas to enable the collection of data using different scan modes. To minimize the reliance on the wheels (and thus the ground) for positioning the antennas, a gantry-type system has been employed to move the antennas parallel to the ground. High precision and repeatability can be achieved using a combination of motors and encoders.

Name: GPR Mapping Robot, Final Public Report	Version: Final, Rev. A
Document ID: GPR-TR-003P	Date: 2/4/2022

The antenna platform has been designed to scan large areas and achieve high positional accuracy of the GPR antenna, ensuring the generation of high accuracy maps. The degrees of freedom offered by the platform design incorporates the following capabilities and functionalities:

Two scanning modes are implemented

1. Common offset mode (Figure 16)
  - a. As the start point, Tx and Rx are moved to the same end. The centers of Tx and Rx are of the same X-position.
  - b. Tx and Rx are moved in tandem from one end to the other. This is called a line-scan.
  - c. Tx and Rx are moved to the next X-position by a step size, usually 50mm.
  - d. Repeat step b and c until 9 line-scans are obtained where the maximum reach in X-direction is reached.

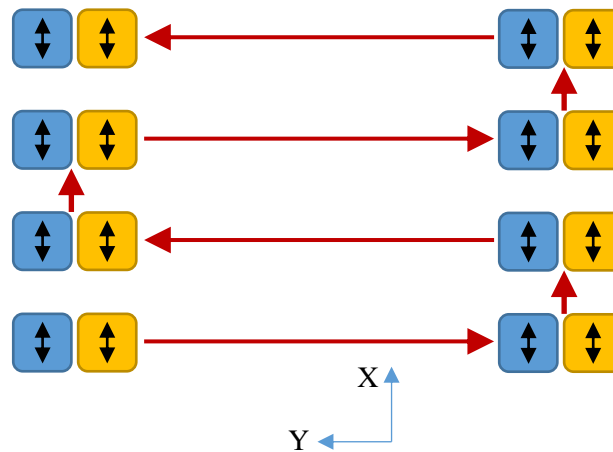


Figure 16. The movement of antenna in the common offset mode. Tx: blue, Rx, yellow.

2. Multi-static mode (Figure 17)
  - a. As the start point, Tx and Rx separate in X-direction using the mini-X and then move to the same end.
  - b. Rx moves from one end to the to the other while Tx remain immobile.
  - c. Tx moves one step in Y-direction.
  - d. Repeat step b and c until Tx reaches the other end.

Name: GPR Mapping Robot, Final Public Report	Version: Final, Rev. A
Document ID: GPR-TR-003P	Date: 2/4/2022

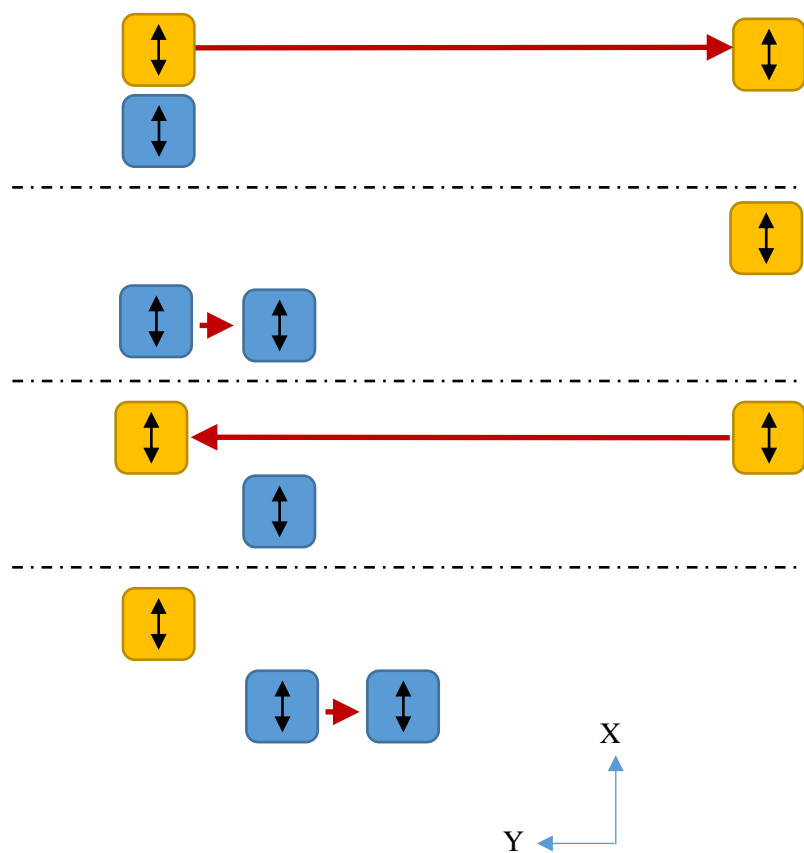


Figure 17. The movement of antenna in the multi-static mode. Tx: blue, Rx, yellow.

The **Mobile platform**, as shown in Figure 15, provides structural support for the antenna platform, transports the antenna platform, and houses electronics, batteries, and the sensors that are used for localization and collision avoidance. It has been designed to drive in rural, sub-urban, and urban areas.

The back side of the robot shown in Figure 18 houses the Li ion batteries and all the electronics which are covered by an aluminum sheet to protect them from dust and other objects. The robot has been designed to have two computers – one for navigation and collision avoidance, and the second one for supporting GPR control and data logging as well as robot control using a CAN bus interface. The robot has been designed for integration of numerous sensors including ultrasonic range sensors, Lidars, and Radars.

Name: GPR Mapping Robot, Final Public Report	Version: Final, Rev. A
Document ID: GPR-TR-003P	Date: 2/4/2022



Figure 18: Back Side of Robot: Showing Batteries

Collision avoidance allows the robot to operate in urban environments and in the vicinity of an operator. While design and sensor selection were completed for collision avoidance, the sensors and software were not incorporated onto the robot. Planning was still carried out to determine the number and type of sensors to obtain the appropriate coverage around the robot as reducing blind spots around the robotic platform is an important part of robot design to ensure safe robotic navigation.

During the navigation, it is also important to detect curbs to avoid any damage to the robot. The locations of sensors were determined to provide cliff sensing.

The robot software has been developed to provide the following functionalities:

- 1) Autonomous GPR Scanning
- 2) Graphical User Interface for Operator
- 3) GPR Data Visualization
- 4) Robot Localization
- 5) Robot Navigation

## 6.1 AUTONOMY IN GPR ANTENNA SCANNING

The motivation behind introducing autonomy in moving the GPR antenna to perform the scanning is to reduce time and human effort in operating it manually and to achieve this consistently and accurately for line scans separated by small distances. There are multiple steps involved in moving the antenna to a required position and configuration, and hence developing automation was an optimal approach. The software continuously monitors all the mechanical and electrical states of the joints, active tasks on the antenna platform, and executes suitable actions when the user defined conditions are satisfied.

## 6.2 GRAPHICAL USER INTERFACE

A Graphical User Interface (GUI) has been developed for the operator to control the robot to perform the scanning operations, data processing, and visualization.

Name: GPR Mapping Robot, Final Public Report	Version: Final, Rev. A
Document ID: GPR-TR-003P	Date: 2/4/2022

### 6.3 GPR DATA VISUALIZATION

Features to process and visualize the collected GPR data have been incorporated in the developed GUI while some features will be incorporated during a subsequent phase of work.

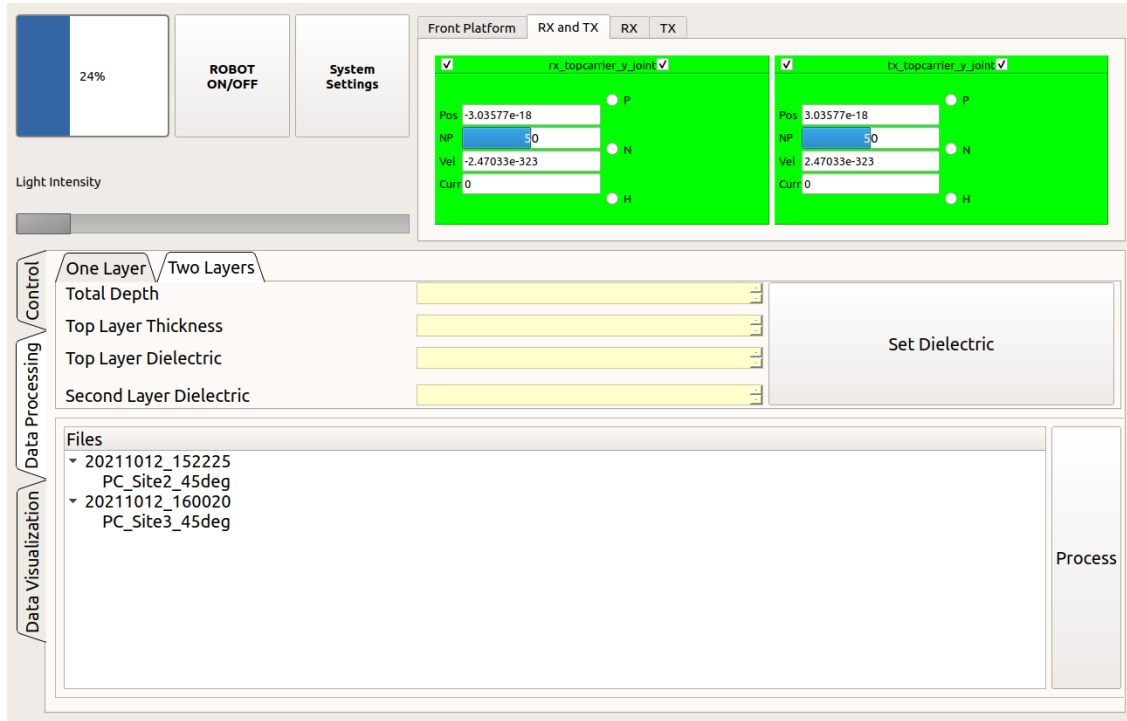


Figure 19: Data Processing tab showing GUI components for two layers

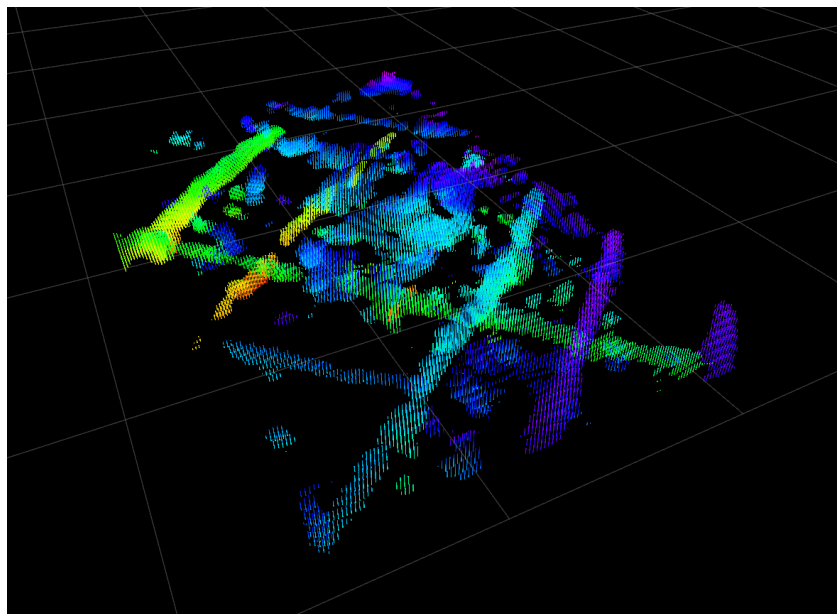


Figure 20: 3D point cloud of the mapped utility - Visualization window

Name: GPR Mapping Robot, Final Public Report	Version: Final, Rev. A
Document ID: GPR-TR-003P	Date: 2/4/2022

## 6.4 LOCALIZATION

The goal of robot localization is to continuously determine the robot's location in the world frame. This provides the reference for controlling the robot trajectory towards its goal location and also determining the geographic coordinates of the utility pipelines being scanned.

Localization is most useful when the robot is moved over long distances such as an entire block in a city or over several city blocks. The GPR testing in this project has been performed over small distances and the use of a localization algorithm was not required. However, the localization feature will be useful when performing automated scanning over longer distances at future test sites and at field sites.

Hence, a probabilistic state estimation method using an Extended Kalman Filter (EKF) available in ROS [8] has been implemented to estimate the robot pose. The EKF module takes vectorized input from different sensors and uses the input covariance to predict the probabilistic location of the robot.

The Simultaneous Localization and Mapping (SLAM) algorithm captures the robot pose using the environment features sensed through Lidars mounted on the robot. It removes the drift developed in dead reckoning through sub-maps matching process. This ensures, that at any given time the cumulative errors are minimal. If an algorithm such as SLAM was not used then the accumulative errors from the IMU and wheel odometry would cause continuous drifting in the estimated position as travel distance increased. GNSS also serves as a reference for correction however SLAM is most useful in localizing the robot in environment where GNSS signals are weak or the accuracy of the GNSS position is not acceptable. SLAM is also used to generate a 2d map (a projected 3d map) of the surroundings which can later be used to map the utility with respect to the environment for visualization. Figure 21 shows the mapped parking lot at ULC Technologies' facility over a distance of approximately 75 meters, which was used to test the performance of the algorithm. It was found that the accuracy of localization after loop closure varied from 40-70 cm. Loop closure (when the robot ends up at the starting point of its travel) provides enhanced accuracy. Even when using the SLAM algorithm, errors will accumulate but through loop closure, the errors are minimized by reducing the uncertainty in position when referencing the starting location.

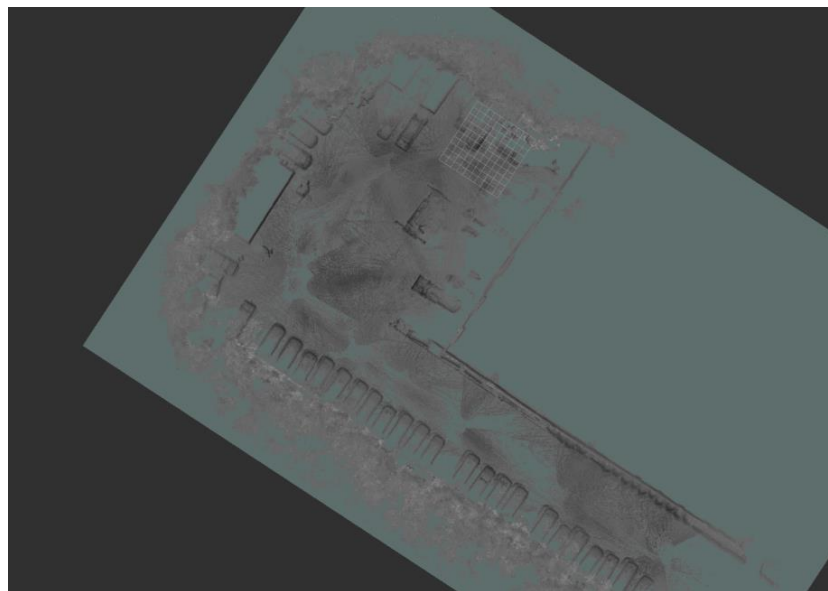


Figure 21: Mapped parking-lot at ULC facility using Google Cartographer

Name: GPR Mapping Robot, Final Public Report	Version: Final, Rev. A
Document ID: GPR-TR-003P	Date: 2/4/2022

The overall accuracy of locating the robot after sensor fusion in the world frame is observed to be under 40 cm. This is the above-ground accuracy. When the robot locating accuracy is combined with the locating accuracy of the GPR, a total accuracy number can be derived. Operators are seeking a total accuracy of less than 24” while some are seeking better accuracy typically around 18”. Additional testing through integrating the robot localization with radar image data location in future work will enable the determination of the total locating accuracy and this can be further improved through tuning of the localization algorithm. The current value of 40 cm (16”) is promising as it is not far off from the total operator required accuracy and there are opportunities to improve the 16” robot locating accuracy.

## **6.5 NAVIGATION**

The purpose of incorporating autonomy in navigation is to perform the scanning operations with minimal human intervention. This requires introducing capabilities to analyze the obstacles in the environment, driving around them, recovering from local minima created by the obstacles and reaching the destination.

### **6.5.1 LOCAL AND GLOBAL COSTMAP**

A 2D costmap is produced using the 3D occupancy grid map generated by voxels of point cloud data from the Lidars. The costmap holds the information about navigable space around the immediate proximity of the robot (Local Costmap) and stores it in a long-term memory (Global Costmap) to plan the trajectory waypoints to reach its destination. This, along with the path planning algorithm, ensures that the robot never collides with an obstacle while moving. Each grid box can hold one of the three values- free (0), occupied (1) and unknown (2).

### **6.5.2 LOCAL AND GLOBAL PLANNER**

The Global planner is the path planning algorithm that uses the global costmap to generate a trajectory to reach the goal location. This generated path (waypoints) is then fed to the local planner which outputs the velocity and orientation to the robot to move towards the goal. The global planner generates a new plan to reach the goal when the occupancy costmap updates during the navigation.

The local planner of the robot uses the inputs from the global planner and local costmap to create a kinematic trajectory of the robot. It generates a value function by evaluating the discretely sampled grid boxes based on:

- a) Proximity to obstacles
- b) Proximity to goal
- c) Proximity to the generated global path plan

This value function encodes the cost of navigating through the grid cells, which in turn generates linear velocities in X & Y directions and angular velocity in the Z direction to move the robot. These values are then used by the differential drive controller to generate velocity commands for each wheel motor on the robot.

### **6.5.3 RECOVERY BEHAVIOR**

During navigation, there are instances in which an obstacle or a group of obstacles create a scenario where the robot gets stuck or continuously oscillates to reach the global path for a certain amount of time. To prevent this, a rotate recovery behavior is incorporated in the robot which, gets it out of the local minima. This characteristic ensures that the robot continues to navigate to reach its goal location. The performance of this feature will be tested in the future after completion of this project.

Name: GPR Mapping Robot, Final Public Report	Version: Final, Rev. A
Document ID: GPR-TR-003P	Date: 2/4/2022

## 7 TESTING AT MOCK ROADWAY

### 7.1 MOCK ROADWAY CONSTRUCTION

#### 7.1.1 MOCK ROADWAY # 1

The design map and the detailed utility lines are shown in Figure 22 and Table 2. The pipe diameters vary from 2” to 12” for steel pipes and 2” to 8” for HDPE pipes. There are also electrical wires in the plastic conduits. The depth of lines varies from 1 to 4 ft. The soil is clayey soil with a 9” concrete surface.

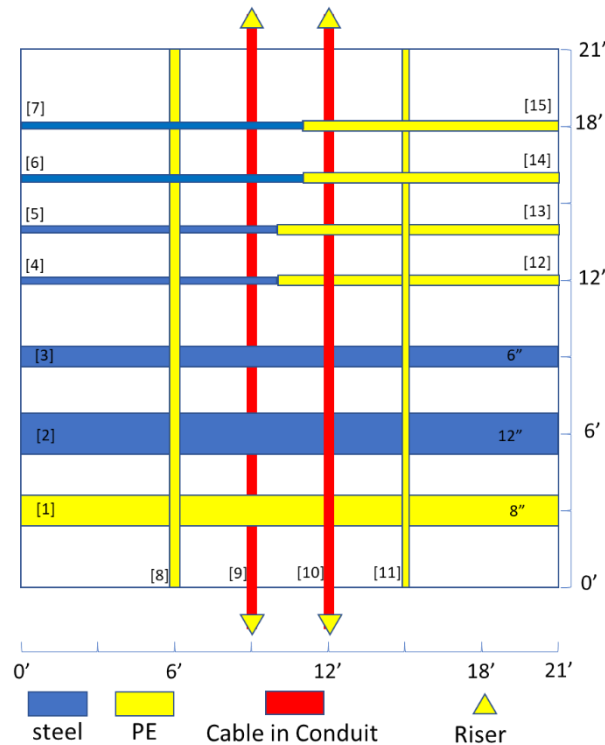


Figure 22. The design map of Mock Roadway #1.

Table 2. Details of the utility lines in Mock Roadway #1.

No.	Diameter (in)	Depth (ft)	Matl.
1	8	3	HDPE
2	12	3	Steel
3	6	3	Steel
4	2	3	Steel
5	2	2	Steel
6	2	1	Steel
7	2	1	Steel
8	3	1.5	HDPE
9	2	4	Cable in HDPE
10	3	2.5	Cable in HDPE

Name: GPR Mapping Robot, Final Public Report	Version: Final, Rev. A
Document ID: GPR-TR-003P	Date: 2/4/2022

No.	Diameter (in)	Depth (ft)	Matl.
11	2	1.5	HDPE
12	3	3	HDPE
13	3	2	HDPE
14	3	1	HDPE
15	3	1	HDPE

### 7.1.2 MOCK ROADWAY #2

ULC completed the construction of a mock roadway test site, where different pipes were buried. The pipe layout, shown in Figure 23, has different levels of complexity; it was designed to create an environment that represents the varying complexity levels in urban areas. The test site has an overall size of 23'x32'. All the pipes were buried in the sandy soil at depths varying between 1.5' and 5'.

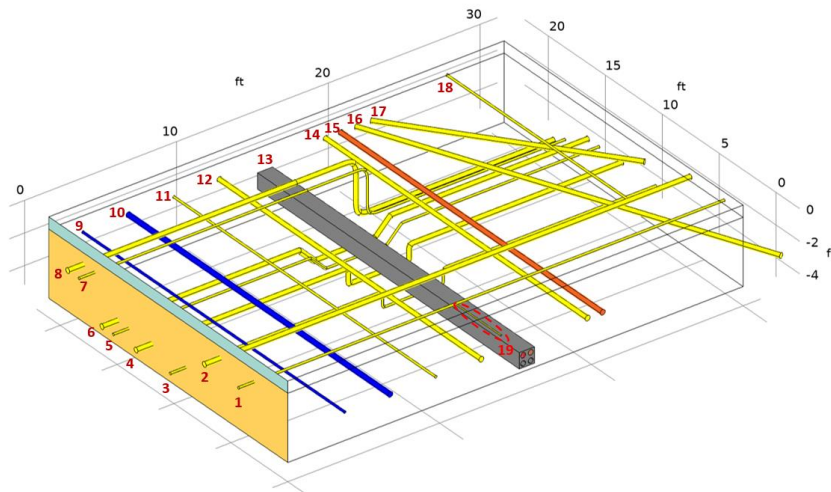


Figure 23: The pipe layout of ULC's mock roadway #2. The pipes numbering scheme is shown in Table 1

The pipes' details are listed in Table 1. PE pipes, steel pipes, and concrete conduits were used to create the underground pipe map. The pipe diameters varied between 1" OD and 4" OD, and the concrete conduit section was built to a 2x2 assembly.

Table 1. Details of the pipes used to build mock roadway #2.

No.	Diameter (in)	Pipe Depth (ft)	Material
1	2"	1.5	HDPE
2	4"	1.5	HDPE
3	2"	3.5-4.5	HDPE
4	4"	3.5-4.5	HDPE
5	2"	3.5-4.5	HDPE
6	4"	3.5-4.5	HDPE
7	2"	1.5-4.5	HDPE

Name: GPR Mapping Robot, Final Public Report	Version: Final, Rev. A
Document ID: GPR-TR-003P	Date: 2/4/2022

No.	Diameter (in)	Pipe Depth (ft)	Material
8	4"	1.5-5	HDPE
9	2"	2.5	Steel
10	4"	2.5	Steel
11	2"	2.5	HDPE
12	4"	2.5	HDPE
13	4"	3.5	Concrete duct bank with electric cable
14	4"	2.5	HDPE
15	4"	2.5	Cable in HDPE
16	4"	2.5	HDPE
17	4"	2.5	HDPE
18	2"	1.5	HDPE
19	1"	1.5	HDPE

Two different types of electric wires, namely a 4/0 aluminum wire and a tracing wire, were passed through the electric conduits. Elbows were used, and electrofusion was performed to form the PE pipes with 90-degree sections.

A tracer wire was installed on top of one of the PE pipes. In addition, pipe risers, extending a few feet above the concrete layer, were connected to the buried pipes to better locate them. Figure 13 shows various stages of construction. The surface of the test site is made of concrete, as shown in Figure 14.

## 7.2 TESTING RESULTS

The robotic platform was tested on Mock Roadway #1 and #2. The common-offset mode was used to scan different areas. The multi-static mode was used to scan lines only since it takes more time than the common-offset mode.

### 7.2.1 COMMON-OFFSET MODE

#### 7.2.1.1 RESULTS ON MOCK ROADWAY #1

The result of the scan of a portion of the roadway is shown as a point cloud in Figure 24. All the pipes in this area were detected successfully. Two HDPE pipes showed reflection weaker than steel pipes and the point cloud is not continuous. But with the help of 3D shape, these two pipes can still be easily identified.

Figure 25 shows the C-scan results at different depths.

Name: GPR Mapping Robot, Final Public Report	Version: Final, Rev. A
Document ID: GPR-TR-003P	Date: 2/4/2022

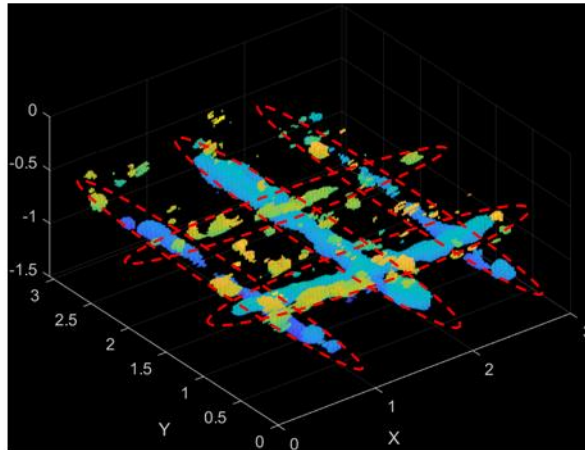


Figure 24. The result in the point cloud format

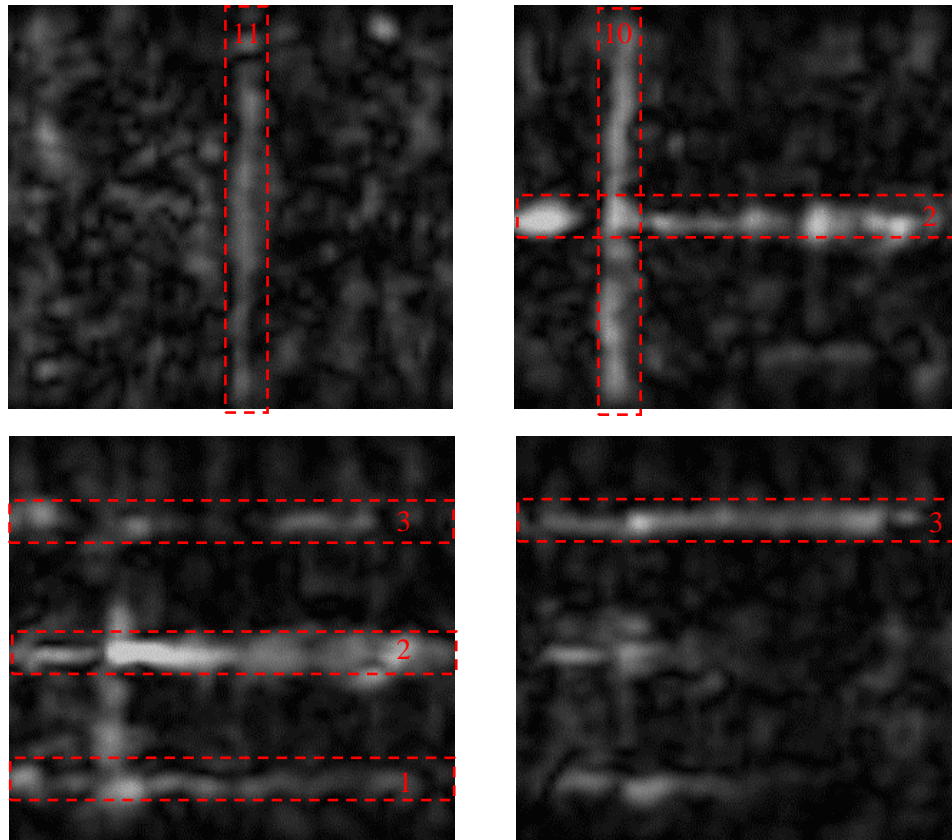


Figure 25. C-scan results at different depths.

In a second portion of the roadway, all pipes were detected including a HDPE pipe at 3ft depth, of only 3” diameter. A conduit was not detected because it was deeper at 4ft depth and was blocked by multiple pipes on top of it.

Name: GPR Mapping Robot, Final Public Report	Version: Final, Rev. A
Document ID: GPR-TR-003P	Date: 2/4/2022

In the third portion of the roadway, the scanning and robot moving direction were intentionally set to be about 45° relative to all the pipes. The scan successfully detected and imaged the angled pipe without any distortion.

To make a comparison, the 3D raw data was (1) directly used as the input for the 2D migration algorithm, and (2) downsampled in the Y direction from  $dy=0.05\text{m}$  to  $dy=0.15\text{m}$  and used as the input for the 2D migration algorithm. The 2D migration results of two  $dy$  values are shown in Figure 26. The pipes that can be seen easily in 3D migration results become difficult to identify in 2D.

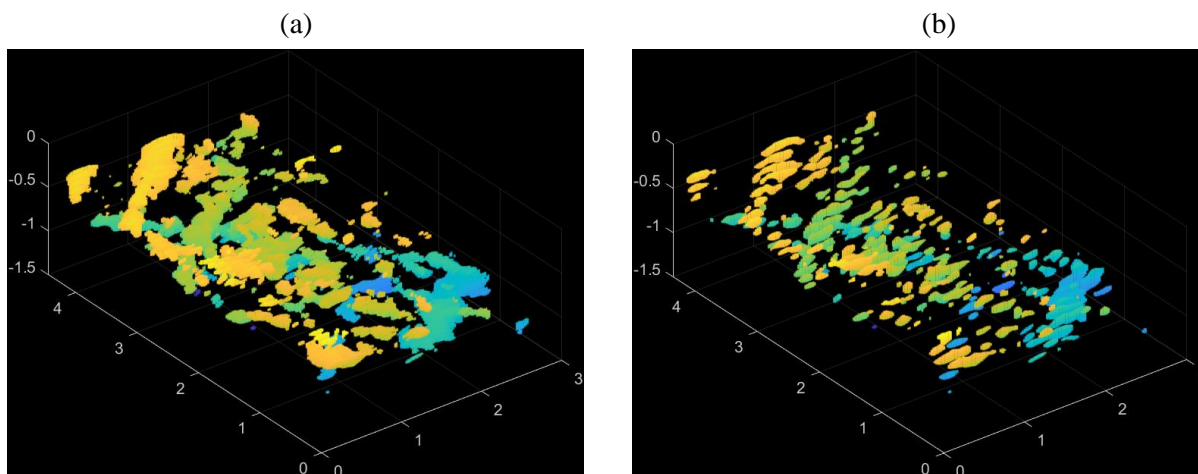


Figure 26. The point cloud results from 2D migration for the 3<sup>rd</sup> scan at site #2 with (a)  $dy=0.05\text{m}$  and (b)  $dy=0.15\text{m}$ .

The C-scan results from 2D migration ( $dy=0.15$ ) are shown in Figure 28 to make a comparison. It is observed that the contrast and focusing become much worse than the 3D migration results. Considering the similarity between the 2D migration in this project and the typical GPR survey in the real world, it is expected that the 3D migration could provide a noticeable improvement to the current GPR system.

Name: GPR Mapping Robot, Final Public Report	Version: Final, Rev. A
Document ID: GPR-TR-003P	Date: 2/4/2022

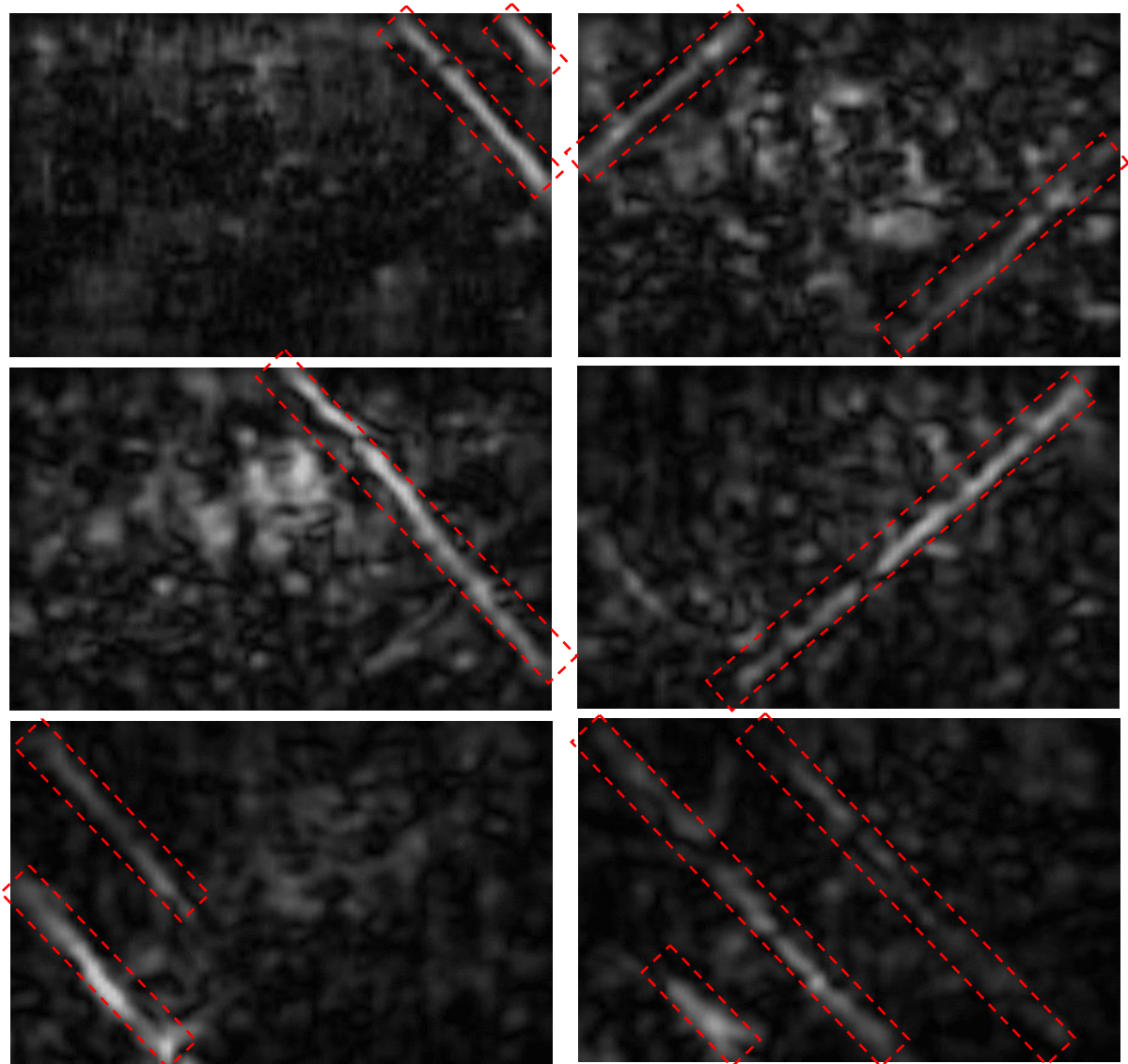


Figure 27. C-scan results from 3D migration at different depths.

Name: GPR Mapping Robot, Final Public Report	Version: Final, Rev. A
Document ID: GPR-TR-003P	Date: 2/4/2022

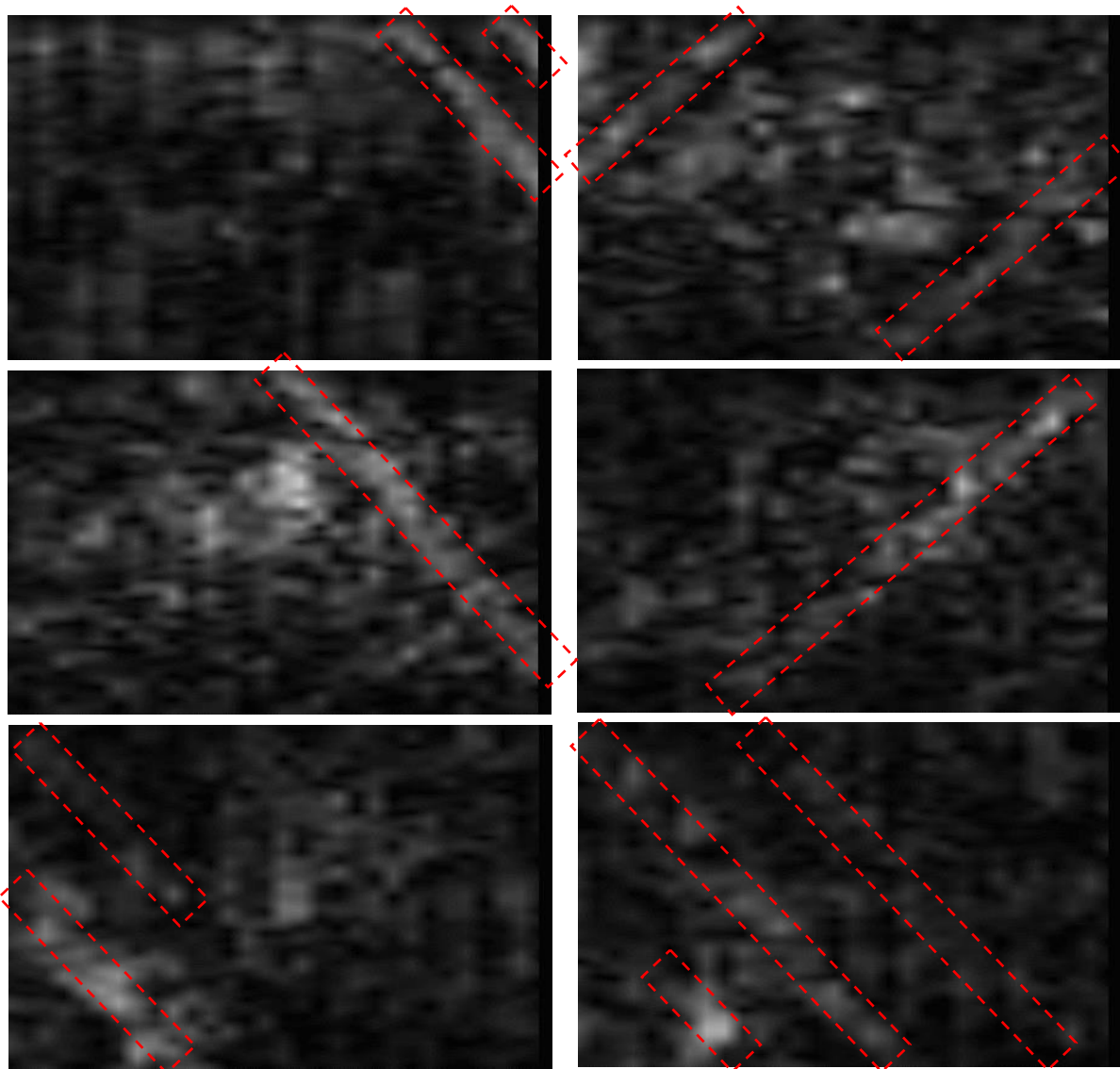


Figure 28. C-scan results from 2D migration ( $dy=0.15m$ ) at different depths.

### 7.2.1.2 RESULTS ON MOCK ROADWAY #2

Mock Roadway #2 has sandy soil. Sand is usually considered as a soil more friendly to GPR than clay soil because it usually induces less attenuation and allows radar waves to penetrate deeper. However, it should be noted that the combination of sand and plastic pipe makes it more challenging for GPR in terms of reflectivity because sand has a permittivity closer to the air and thus produces less reflection. For shallow objects, i.e. utility lines, reflectivity is a more dominant factor than soil attenuation. So non-metallic pipes in sandy soil are not necessarily easier targets than those in clay soils.

A scanned area and the point cloud results are shown in Figure 29. From the point cloud, multiple pipes can be identified. To examine the results in more detail, the C-scan results are used in Figure 30. Two pipes

Name: GPR Mapping Robot, Final Public Report	Version: Final, Rev. A
Document ID: GPR-TR-003P	Date: 2/4/2022

that were just 1ft apart can still be easily differentiated which confirms the resolution of the imaging algorithms.

A 1” HDPE pipe was not detected because the air volume is too small to induce sufficient reflection. A 2” diameter pipe buried at 3.5 ft was not detected.

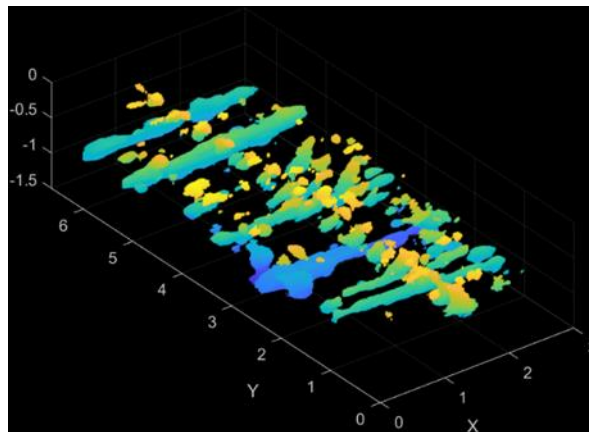


Figure 29. The 3D migration results in the point cloud format

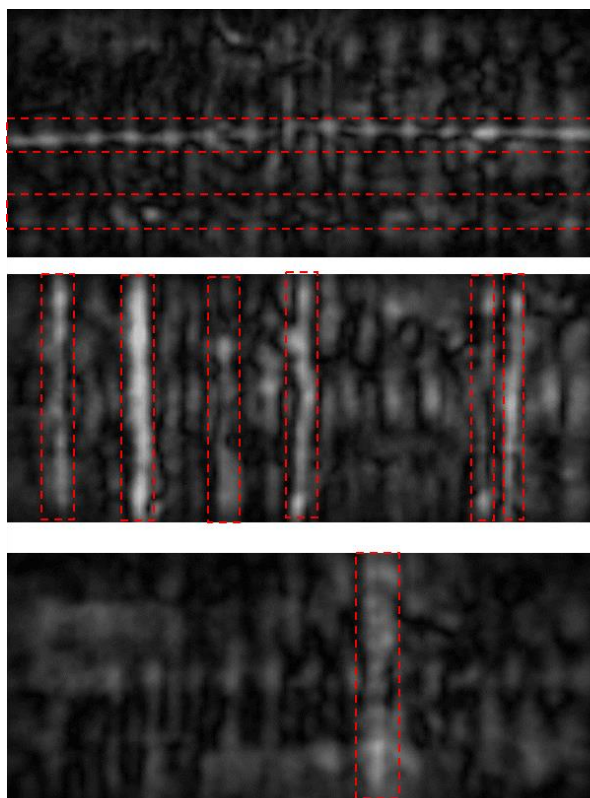


Figure 30. C-scan results from 3D migration at different depths.

Name: GPR Mapping Robot, Final Public Report	Version: Final, Rev. A
Document ID: GPR-TR-003P	Date: 2/4/2022

### 7.2.2 MULTI-STATIC MODE

A portion of the site was chosen for multi-static data collection. The processed results in real numbers and absolute values are shown in Figure 31 for common-offset and multi-static data. The amplitude in each figure is normalized by the maximum value of itself. It is seen that both methods have a similar capability to detect pipes within the range of plotting which agrees with the findings in the numerical simulation study. It is also observed that the multi-static result has less clutter and noise than the common-offset result which is because of the multi-angle view used by the multi-static data collection.

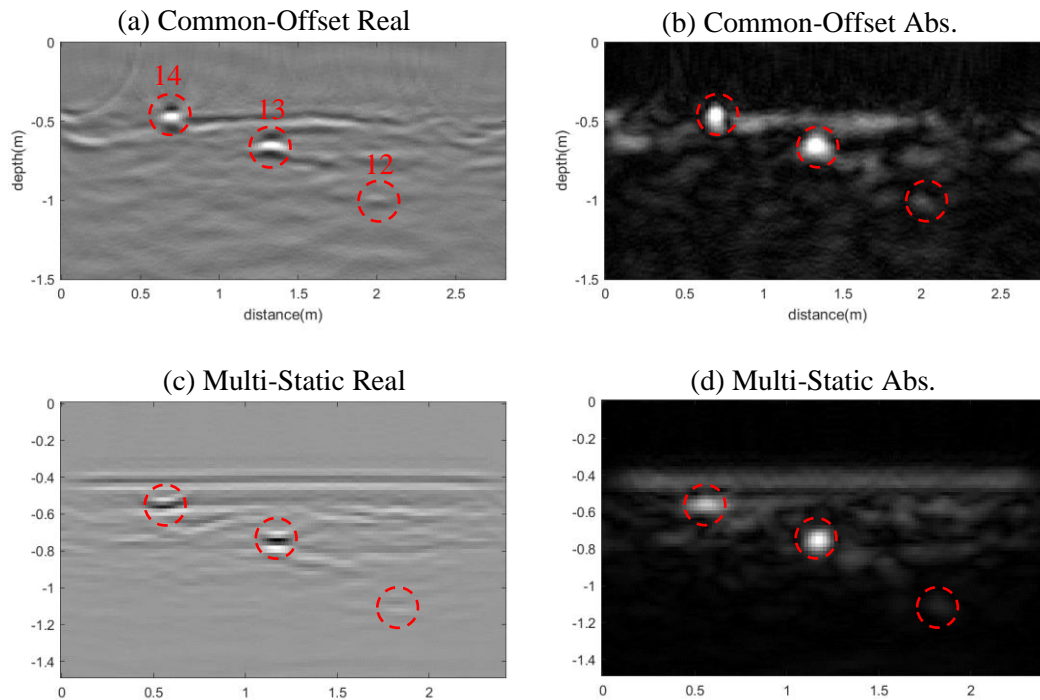


Figure 31. Comparison between the results from common-offset and multi-static data collection in real and absolute values.

### 7.3 SUMMARY

To summarize the work of testing the GPR mapping robot, the following highlights are listed

1. The function of the robot to conduct common offset and multi-static scanning modes has been tested and validated successfully.
2. The common-offset mode with fine grid size (50mm) has been proved to produce high accuracy and resolution imaging of the underground utilities. Its advantage over the sparse scanning path used in the current GPR survey has been demonstrated.
3. By using the GPR mapping robot, the non-metallic pipes (HDPE) can be detected at the following conditions.

Name: GPR Mapping Robot, Final Public Report	Version: Final, Rev. A
Document ID: GPR-TR-003P	Date: 2/4/2022

Table 3. Detected utility lines during the project.

Soil	Pipe Diameter (in)	Depth (ft)
Clay	8	3
Clay	3	1
Clay	3	1.5
Clay	3	2
Clay	3	3
Clay	2	1.5
Sand	4	1.5
Sand	4	2.5
Sand	2	1.5
Sand	2	2.5

- The multi-static data showed imaging results with less noise and clutter than the common-offset data.
- Testing of the robot localization indicates the ability to achieve approximately 16” of robot positioning accuracy in the absence of reliable GNSS signals.

#### 7.4 FUTURE WORK

Based on the knowledge and results obtained during the project, the following future work could be considered.

- More tests should be conducted using the multi-polarization configuration and the vector-form C-scan results.
- Test the common offset and multi-static scanning in real-world scenarios to further evaluate its performance.
- Use antennas of other specifications to amplify the capability to detect deeper targets.
- Improve the ground coupling of the antenna to further improve the consistency and quality of raw data.
- Integrate robot localization with GPR image coordinates to provide accurate locations of the underground pipe referenced to the robot origin and convert coordinates to a chosen Geographical Information System such as ESRI.
- Test and validate robot navigation to support autonomous operations of the robot in the presence of obstacles.
- Integrate the selected collision avoidance sensors with the robot and test using the navigation algorithms for safe operations in the presence of humans and property.

Name: GPR Mapping Robot, Final Public Report	Version: Final, Rev. A
Document ID: GPR-TR-003P	Date: 2/4/2022

## 8 REFERENCES

1. A. Giannopoulos, *Modelling ground penetrating radar by GprMax*. Construction and Building Materials, 2005. **19**(10): p. 755-762.
2. C. Warren, A. Giannopoulos, and I. Giannakis. *An advanced GPR modelling framework: The next generation of gprMax*. in *2015 8th International Workshop on Advanced Ground Penetrating Radar (IWAGPR)*. 2015.
3. J. M. Lopez-Sanchez and J. Fortuny-Guasch, *3-D radar imaging using range migration techniques*. IEEE Transactions on Antennas and Propagation, 2000. **48**(5): p. 728-737.
4. A. J. Hunter, B. W. Drinkwater, and P. D. Wilcox, *The wavenumber algorithm for full-matrix imaging using an ultrasonic array*. IEEE Transactions on Ultrasonics, Ferroelectrics, and Frequency Control, 2008. **55**(11): p. 2450-2462.
5. X. Zhuge and A. G. Yarovoy, *Three-Dimensional Near-Field MIMO Array Imaging Using Range Migration Techniques*. IEEE Transactions on Image Processing, 2012. **21**(6): p. 3026-3033.
6. Chen Chi-Chih, et al., *Ultrawide-bandwidth fully-polarimetric ground penetrating radar classification of subsurface unexploded ordnance*. IEEE Transactions on Geoscience and Remote Sensing, 2001. **39**(6): p. 1221-1230.
7. Douglas S. Sassen and Mark E. Everett, *3D polarimetric GPR coherency attributes and full-waveform inversion of transmission data for characterizing fractured rock*. GEOPHYSICS, 2009. **74**(3): p. J23-J34.